

**Mantle-driven Uplift of Hangai Dome: New Seismic Constraints from Adjoint**

**Tomography**

Min Chen<sup>1\*</sup>, Fenglin Niu<sup>1,2</sup>, Qinya Liu<sup>3</sup>, Jeroen Tromp<sup>4,5</sup>

<sup>1</sup>Department of Earth Science, Rice University, Houston, Texas, USA.

<sup>2</sup>State Key Laboratory of Petroleum Resource and Prospecting, and Unconventional Natural Gas

Institute, China University of Petroleum, Beijing, China.

<sup>3</sup>Department of Physics, University of Toronto, Toronto, Ontario, Canada.

<sup>4</sup>Department of Geosciences, Princeton University, Princeton, NJ, USA.

<sup>5</sup>Program in Applied and Computational Mathematics, Princeton University, Princeton, NJ, USA.

\*Correspondence: [min.chen@rice.edu](mailto:min.chen@rice.edu)

**Contents of this file**

Text S1 to S4

Figures S1 to S11

References

**Additional Supporting Information (File uploaded separately)**

Movie S1 (MovieS1\_Hangai\_Dome\_LowRes.avi)

## 37 **Text S1. Adjoint tomography and model construction**

38 Different from traditional ray-theory based tomography, adjoint tomography takes  
39 into account full 3-D wave propagation effects and off-ray-path sensitivity. In this  
40 application, we use a spectral-element method (SEM) to simulate 3-D seismic wave  
41 propagation [*Komatitsch and Tromp, 2002a, 2002b*] and to calculate finite-frequency  
42 sensitivity kernels for iterative tomographic inversion [*Tromp et al., 2005; Liu and*  
43 *Tromp, 2006, 2008; Tape et al., 2009; Zhu et al., 2012*]. Technical details of constructing  
44 the East Asia Radially Anisotropic Model (EARA2014) are described in a previous  
45 publication [*Chen et al., 2015*]. Here, we only provide a short summary of the data and  
46 methods. Our tomographic procedure consists of first re-inverting source parameters and  
47 then iteratively refining the 3-D structure based on finite-frequency sensitivity kernels.

48 We select an initial model that combines 3-D global radially anisotropic mantle  
49 model S362ANI [*Kustowski et al., 2008*] with 3-D crustal model Crust2.0 [*Bassin et al.,*  
50 *2000*]. The initial earthquake source parameters are given by the centroid moment-tensor  
51 (CMT) solution [*Ekström et al., 2005*]. Our 3-D models have an isotropic  
52 parameterization in the crust and in the mantle below the transition zone, and a radially  
53 anisotropic parameterization between the Moho and the 660 km discontinuity. The SEM  
54 mesh incorporates a 4-min model of topography created by subsampling and smoothing  
55 ETOPO-2 [*National Geophysical Data Center, 2006*] as well as undulations of the Moho  
56 [*Bassin et al., 2000*] and the 410 km and 660 km discontinuities [*Kustowski et al., 2008*].

57 From the global CMT solution database we selected 227 earthquakes ( $M_w=5-7$ ) (red  
58 stars in Figure 1, inset) with good signal-to-noise-ratio records for both source and  
59 structural inversions. Source parameters are reinverted within the initial structural model

60 using the CMT3D inversion method [Liu *et al.*, 2004]. In order to obtain good azimuthal  
61 data coverage for the source inversion, we used seismic waveforms from five high-  
62 quality global and regional seismic networks (IU, II, G, GE, and IC).

63 After the source inversions, we updated the 3-D structure based on finite-frequency  
64 kernels with fixed source parameters. In our structural inversion, the model is  
65 parameterized on the SEM Gauss-Lobatto-Legendre integration points, which have an 8  
66 km lateral spacing and a vertical spacing of less than 5 km in the crust, and a 16 km  
67 lateral spacing and an average vertical spacing of  $\sim 10$  km in the upper mantle. Our data  
68 set for structural inversion consists of three-component waveforms recorded by 1,869  
69 stations from F-net, CEArray [Zheng *et al.*, 2009], NECESSArray, INDEPTH IV Array,  
70 and other regional and global seismic Networks (yellow triangles in Figure 1, inset).

71 Synthetic seismograms for the initial 3-D model and subsequent updated models were  
72 calculated for all stations (Figure 1, inset). Measurement windows are selected in three  
73 passbands, namely, 15 s–40 s (short-period passband), 30 s–60 s (intermediate-period  
74 passband), and 50 s–100 s (long-period passband) for the first 12 iterations. In subsequent  
75 iterations we lowered the lower bounds of these passbands to 12 s, 20 s, and 40 s,  
76 respectively. Selecting measurement windows is accomplished based on FLEXWIN  
77 [Maggi *et al.*, 2009], an algorithm to automatically pick measurement windows in  
78 vertical, radial, and tangential component seismograms by comparing observed and  
79 synthetic seismograms. Frequency-dependent traveltimes misfits are measured within the  
80 chosen windows. Adjoint sources are constructed using traveltimes misfit measurements  
81 for all picked phases, e.g., body wave phases (direct P and S, pP, sP, sS, pS, PP, and SS)  
82 and surface waves (Rayleigh and Love). The adjoint sources assimilate the misfit as

83 simultaneous fictitious sources, and the interaction of the resulting adjoint wavefield with  
84 the regular forward wavefield forms the event kernels. All event kernels are summed to  
85 obtain the gradient or Fréchet derivative, which is preconditioned and smoothed for a  
86 conjugate gradient model update. The optimal step length for the model update is chosen  
87 based on a line search. The updated model is used as the starting model for the next  
88 iteration of further structural refinement. The same procedure is repeated until no  
89 significant reduction in misfit is observed, in our case after 20 iterations.

## 90 **Text S2. Model quality assessment**

91 Detailed assessments of model EARA2014 are described in a previous publication  
92 [*Chen et al.*, 2015]. This section provides additional quality assessments targeted to the  
93 model region beneath Hangai Dome.

94 We performed “point-spread function” (PSF) resolution tests targeting the deep LV2  
95 feature observed beneath Hangai Dome. The PSF test evaluates the resolution of a  
96 particular point of interest in the model by the degree of “blurring” of a perturbation  
97 located at that point, and by revealing the tradeoff with other model parameters [*Fichtner*  
98 *and Trampert*, 2011; *Zhu et al.*, 2012]. We placed a spherical anomaly represented by a  
99 3D Gaussian function centered at 300 km beneath Hangai Dome, with a 120 km radius  
100 and a minimal  $-4\%$  perturbation in  $V_{SH}$  (Figure S1a) or maximal  $4\%$  perturbation in  $V_{SV}$   
101 (Figure S2a). Although there is certain degree of smearing (Figures S1b and S2c), the  
102  $V_{SH}$  and  $V_{SV}$  PSFs recover the main features at comparable resolution, while showing  
103 negligible tradeoff with other parameters (Figures S1c, S1d, S2b, and S2d).

104 Compared to the initial model, final model EARA2014 predicts 3-D wave  
105 propagation much better in the Hangai Dome area as illustrated in Figure S3, which

106 shows examples of waveform fitting for station HD25 at central Hangai (PASSCAL  
107 network XL) for a shallow earthquake (25.9 km depth, 201207302230A) in southern  
108 Siberia. Both the station and the event are not used in the inversion, and thus the  
109 seismograms serve as independent data to benchmark the 3-D model. We calculated  
110 synthetic seismograms for both the initial model and the final model (EARA2014) using  
111 the spectral-element solver SPECFEM3D\_GLOBE. The observed seismograms and two  
112 model synthetics are bandpass filtered in period ranges of 12 s–40 s and 20 s–60 s.  
113 Waveform fits between the data and EARA2014 synthetics shows an overall  
114 improvement in both period ranges on all three components relative to the fits of the  
115 initial model.

### 116 **Text S3. Model analysis**

117 In order to better understand the seismic features in model EARA2014, we selected  
118 three sampling regions that are representative of Hangai Dome, Hentai Dome, and the  
119 Siberia craton (Figure S4a). The means of each sampling region as well as the entire  
120 Hangai-Hentai-Baikal area are calculated at each depth for  $V_{SV}$  (Figure S4b),  $V_{SH}$  (Figure  
121 S4c),  $V_S$  (Figure S4d), and radial anisotropy (Figure S4e). Depth profiles of various  
122 seismic properties exhibit distinct characteristics for each region (Figure S4). At depths  
123 shallower than 150 km, compared to the regional mean, Siberia has higher wavespeeds  
124 and weakly positive radial anisotropy (~0.5%), while the Hangai and Hentai areas have  
125 lower seismic wavespeeds and strongly positive radial anisotropy (up to 4% or 5%)  
126 (Figures S4b, S4c, and S4d). However, the Hangai area appears to have much lower  
127 wavespeed anomalies and more strongly positive radial anisotropy than the Hentai area.  
128 In particular, between the Moho (~50 km) and 90 km depth, very low wavespeeds ( $V_{SV}$

129 or  $V_s$  less than 4.2 km/s) appear beneath the Hangai area (Figures S4b, S5a, S5b, and  
130 S5c), which suggests the existence of partial melt, possibly caused by decompression  
131 melting (Figure 4). The strongly positive radial anisotropy (>4%) in the same depth range  
132 (~50 km–90 km) (Figures S4e and S5d) supports our hypothesized horizontal migration  
133 of partial melt (Figure 4).

134 High topography (ETOPO1) [Amante and Eakins, 2009] and low Bouguer gravity  
135 anomalies [Balmino et al., 2012] are well correlated in the Hangai Dome area (Figures  
136 S6a and S6b). Low Bouguer gravity anomalies can be explained in terms of a thickened  
137 crust, and mass deficit in the crust or mantle. There are observations of thickened crust  
138 (42 km–57 km with an average of ~ 50 km) [Stachnik et al., 2014] beneath the Hangai  
139 area from a regional dense seismic array. However accounting for the observed Bouguer  
140 gravity anomalies with an Airy-type deep crustal root would require an overthickened  
141 crust of ~ 60 km [Petit et al., 2002]. The remaining gravity residual not explained by  
142 crustal thickening has to be caused by a mass deficit in the crust or mantle [Petit et al.,  
143 2002].

144 There are two mechanisms that might lead to crustal thickening: tectonic driven  
145 crustal shortening and magmatic underplating causing addition of basalt at the bottom of  
146 the crust. Geodetic modeling suggests no significant neotectonic deformation due to the  
147 remote India-Asia collision at Hangai Dome [Liu and Bird, 2008]. Therefore, tectonic  
148 driven crustal shortening at Hangai Dome might be insignificant. The viable mechanism  
149 of crustal thickening could be due to magmatic underplating [McKenzie, 1984].

150 Airy isostasy requires  $\Delta h \rho_c = (\rho_m - \rho_c)(\Delta H - \Delta h)$ , where  $\Delta h$  is the surface uplift,  
151  $\Delta H$  the thickness of the additional crust,  $\rho_c$  the underplated gabbroic basalt mass

152 density (assumed to be  $2.7 \text{ Mg/m}^3$ ) [McKenzie, 1984; Cox, 1993], and  $\rho_m$  the upper  
153 mantle peridotite mass density (assumed to be  $3.3 \text{ Mg/m}^3$ ). In the Hangai region, uplift  
154  $\Delta h$  of  $\sim 2 \text{ km}$  requires  $\Delta H$  to be  $\sim 11 \text{ km}$ . If we suppose that the underplated basalt is  
155 more ultramafic with a  $\rho_c$  of  $3.0 \text{ Mg/m}^3$ , then  $\Delta H$  is  $\sim 22 \text{ km}$ . Post-12 Ma basalts at  
156 Hangai are erupted sporadically in small volume and with low melt degree. This limited  
157 surface expression of underlying magma supply makes it unlikely to have an additional  
158 layer of  $\sim 11 \text{ km}$ – $22 \text{ km}$  thick underplated basalt. However, further investigation of  
159 underplated thickness requires robust seismic constraints. The quality of crustal thickness  
160 constraints in CRUST2.0 is not ideal given that it is a low-resolution global crustal model  
161 and does not have good coverage from active source seismic surveys. While keeping 3-D  
162 Moho undulations the same as in CRUST2.0 throughout our adjoint tomographic  
163 inversion, we update mantle and crustal wavespeeds to obtain final model EARA2014.  
164 Un-modeled crustal thickness may have been compensated by low-V near the Moho.  
165 Crust2.0 Moho beneath Hangai Dome is at about  $43 \text{ km}$ . In EARA2014 a low-V zone  
166 with wavespeeds of  $V_{sv}$  less than  $4.2 \text{ km/s}$  (about a 7% reduction) exists beneath Hangai  
167 Dome between  $\sim 50 \text{ km}$ – $90 \text{ km}$  (Figure S4a). The low-V between  $\sim 50 \text{ km}$ – $90 \text{ km}$  depth  
168 could indicate a vertically smeared tomographic version of un-modeled transitional crust  
169 thickened with addition of basalt due to magmatic underplating or/and upper mantle with  
170 partial melt due to asthenospheric upwelling. Future more robust seismic constraints on a  
171 possible underplated basalt layer would require high-resolution seismic imaging of Moho  
172 depth variations and wavespeeds of the crust and uppermost mantle using regional dense  
173 seismic arrays, such as the temporary IRIS/PASSCAL array with 75 stations deployed at  
174 Hangai Dome.

175 Through further model analysis of EARA2014 (Figure 6), we observe that long-  
176 wavelength (~600 km) negative (~100 mGal–250 mGal) Bouguer gravity anomalies  
177 (Figure S6b) in the Hangai Dome area correspond to regions with larger integrated shear  
178 wavespeed reduction in the upper 250 km (>2%) (Figure S6c) and a thicker low-V  
179 column (~100 km) (defined by a larger than 2% shear wavespeed reduction), which both  
180 suggest an overall mass deficit in both the crust and uppermost mantle.

181 Because relative shear wavespeed anomalies ( $\delta \ln V_s$ ) are very well determined by our  
182 study for the crust and upper mantle beneath Hangai, it is very natural to use  $\delta \ln V_s$  as a  
183 proxy for relative density anomalies  $\delta \ln \rho$ . Assuming thermal effects dominate in the  
184 lithosphere, we can scale  $\delta \ln \rho$  to  $\delta \ln V_s$  with a constant factor  $\zeta$  in the upper mantle

$$185 \quad \zeta = \delta \ln \rho / \delta \ln V_s . \quad (1)$$

186 The scaling factor  $\zeta$  in reality varies with depth. In order to keep it simple we only  
187 chose two values of  $\zeta$  for further model analysis: the commonly used  $\zeta = 0.33$   
188 [Anderson, 1987] and  $\zeta = 0.2$  [Karato, 1993], which is the lower bound of  $\zeta$  in the  
189 upper mantle when anelasticity is taken into account. Because the CRUST2.0 Moho  
190 depth is not updated by our inversion, it is not straightforward to use the Airy concept for  
191 model analysis. We instead use the more natural Pratt concept to predict the elevation  
192 change  $\Delta h_p$ . Based on Pratt isostasy,

$$193 \quad \Delta h_p = -H_c \delta \ln \rho , \quad (2)$$

194 where  $H_c$  is the compensation depth. If we assume the bulk density anomaly is an  
195 integrated density anomaly at each depth  $z$ , Equation (2) can also be written as follows:

196 
$$\Delta h_p = -\int_0^{H_c} \delta \ln \rho(z) dz, \quad (3)$$

197 Based on equation (1), we have

198 
$$\Delta h_p = -\zeta \int_0^{H_c} \delta \ln V_s(z) dz. \quad (4)$$

199 Because we are more interested in the relative elevation change in our study region,  
200 we can evaluate the elevation with the mean removed:

201 
$$\Delta h_p - \overline{\Delta h_p} = -\zeta \int_0^{H_c} [\delta \ln V_s(z) - \overline{\delta \ln V_s(z)}] dz, \quad (5)$$

202 where  $\overline{\Delta h_p}$  and  $\overline{\delta \ln V_s(z)}$  are the predicted regional mean elevation and mean shear  
203 wavespeed anomaly at each depth, respectively. Let's denote the predicted elevation  
204 variation (equation (5)) as

205 
$$\delta h_p = -\zeta \int_0^{H_c} [\delta \ln V_s(z) - \overline{\delta \ln V_s(z)}] dz. \quad (6)$$

206 Based on equation (6) we can calculate the predicted elevation variations ( $\delta h_p$ ) in the  
207 entire Hangai-Hentai-Baikal-Altai-Sayan-Tianshan region and also the misfit ( $\delta h_p - \delta h_o$ )  
208 between the predicted  $\delta h_p$  and observed elevation variation  $\delta h_o$ . We tried a set of  
209 parameter combinations amongst two different scaling factors ( $\zeta$ : 0.2 and 0.33) and  
210 three different compensation depths ( $H_c$ : 50 km, 80 km, and 150 km) (Figures 7 and 8).  
211 The best combinations of parameters to predict elevation variations of Hangai Dome  
212 invoking Pratt isostasy are  $H_c$  of 80 km with  $\zeta$  of 0.33 (Figures 8c and 8d) and  $H_c$  of 150  
213 km with  $\zeta$  of 0.2 (Figures 7e and 7f). Both suggest that the compensation depth of  
214 Hangai Dome is much deeper than the Moho, possibly as deep as 150 km. Our

215 calculations ignore buoyancy due to Moho undulations, density anomalies caused by  
216 partial melt or composition, the depth dependence of the scaling factor  $\zeta$ , or any  
217 potential dynamic topography due to mantle convection. But to first order, our model  
218 analysis (Figures 7 and 8) shows that isostatic compensation of surface uplift can be  
219 achieved at Hangai Dome and the large depth of compensation (80 km to 150 km)  
220 implies buoyancy contributions from both the crust and the upper mantle. Misfits of  
221 elevation variations are also small at Hantai Dome and Sayan Mountains (Figures 7f and  
222 8d), indicating these two elevation-highs may also be isostatically compensated.  
223 However, other tectonic units such as Lake Baikal, the Altai Mountains, and the Tianshan  
224 Mountains always show significant misfits, implying Moho undulation and/or dynamic  
225 topography due to mantle convection play more important roles in modulating surface  
226 elevation.

#### 227 **Text S4. Receiver functions**

228 We conducted the following receiver function analysis to investigate possible mantle  
229 transition zone thickness changes due to hot mantle upwelling, i.e., the LV2 feature  
230 observed in EARA2014 beneath Hangai Dome (Figure 3).

231 The receiver functions were collected from two GSN (Global Seismographic  
232 Network) stations, TLY and ULN, and one PASSCAL station, HD25 (Figure S9a). The  
233 3-component teleseismic waveform data were first rotated and projected into P- and SV-  
234 components [Vinnik, 1977; Niu and Kawakatsu, 1998; Niu et al., 2005]. We employed  
235 the ‘water-level’ deconvolution technique [Clayton and Wiggins, 1976] to generate  
236 receiver functions. We selected a 100 s time window (5 s and 95 s before and after the P  
237 wave) to compute the source spectrum of each earthquake. We further screened receiver

238 functions with various methods [*Chen et al.*, 2010] to eliminate noisy data, and selected a  
239 total of 550, 250, and 41 receiver functions at TLY, ULN and HD25, respectively.

240 We applied both single-station and CCP stacking techniques to the receiver-function  
241 data to image the 410-km and 660-km discontinuities as well the transition zone (TZ)  
242 thickness beneath the study area [*Dueker and Sheehan*, 1997; *Gilbert et al.*, 2003; *Niu et*  
243 *al.*, 2005]. To do so, we first ray-traced two converted phases, P410s and P660s, using  
244 the 1D iasp91 velocity model [*Kennett and Engdahl*, 1991] to compute conversion points  
245 at the 410-km and 660-km discontinuities, which are shown by white circles and blue  
246 pluses in Figure S9a, respectively.

247 To compute a simple-stack at the three stations, we first divided the conversion points  
248 into four quadrants and gathered receiver functions based on their quadrant location.  
249 Hereafter we refer this single-station single-quadrant stack as an SSS stack. To determine  
250 the depth of the two discontinuities from the SSS stacks, we first assumed a conversion  
251 depth,  $d$ , and computed the relative arrival time of the converted phase  $Pds$  with respect  
252 to the direct P based on the 3D EARA2014 model [*Chen et al.*, 2015]. The 3D  $Pds$  and P  
253 traveltimes were computed based on approximate 1-D raypaths and 3-D velocity  
254 structures [*Liu et al.*, 2015]. We then summed the N receiver function within a 0.2 s  
255 window centered on the arrival time of  $Pds$  using an  $n^{\text{th}}$ -root stacking technique  
256 [*Muirhead*, 1968]. We varied  $d$  from 200 km to 1,000 km in increments of 1 km. An  
257 example of the SSS stack at the three stations is shown in Figure S10a. The estimated  
258 depth of 410-km is 412 km, 408 km, and 412 km beneath TLY, ULN, and HD25,  
259 respectively, and the measured 660-km depths are 654 km, 643 km, and 654 km,

260 respectively, resulting in a TZ thickness of 242 km, 235 km, and 242 km beneath the  
261 three stations (Figure S10a).

262 We also selected an area around the three stations (white rectangle in Figure S9a) and  
263 applied the CCP stacking technique to map TZ thickness variations beneath the area. We  
264 divided the study area (96°E to 114°E, 45°N to 53°N) into meshed grids of 0.2° by 0.2°,  
265 and used a circular cap with a radius of 1.5 degrees for gathering receiver functions. The  
266 total number of caps is 3,731 (91×41), and there is significant overlap among the caps.  
267 This serves as a low-pass filter that smoothes topographic relief on the two  
268 discontinuities with a corner wavelength roughly equivalent to the size of the caps, i.e.,  
269 ~300 km. We then stacked all receiver functions within a 0.2 s window centered on the  
270 arrival time of *Pds*, which was computed from the 3-D EARA2014 model. An example  
271 of the CCP stacks along latitude 46° north is shown in Figure S10b. We manually picked  
272 the depths of the two discontinuities and the corresponding TZ thickness is shown in  
273 Figure S5b. We observe that a ~10 km–20 km thinner TZ area (Figure S9b) corresponds  
274 to the low wavespeed anomalies inside the TZ beneath station HD25 (Figure S11).

275

276

277

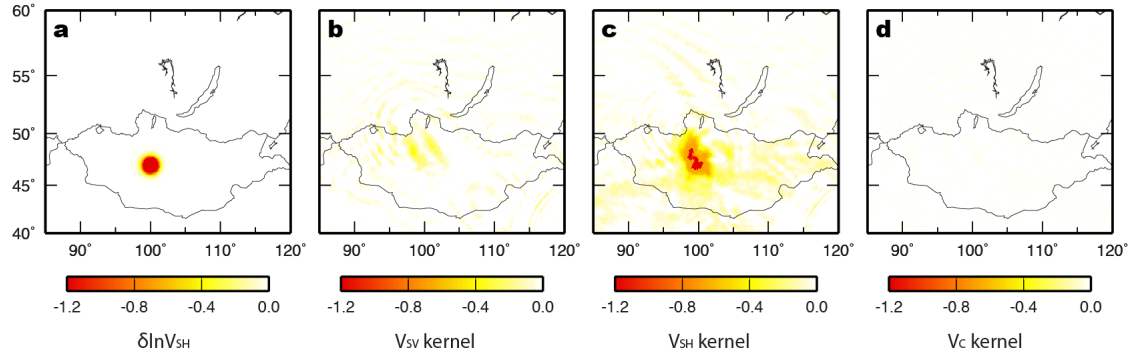
278

279

280

281

282



283

284 **Figure S1.** Resolution test of  $V_{SH}$  beneath Hangai Dome. **a** A 3D Gaussian spherical  
 285 perturbation in  $V_{SH}$  with a minimum strength of  $-4\%$  at the center is placed at a depth of  
 286 300 km while  $V_{SV}$  and  $V_C$  remain unperturbed. **b**  $V_{SV}$  Hessian kernel map indicating  
 287 tradeoff between  $V_{SV}$  and  $V_{SH}$ , where small kernel amplitudes indicate little tradeoff. **c**  
 288  $V_{SH}$  Hessian kernel map showing imaging resolution of  $V_{SH}$ , where a less blurry kernel  
 289 image at the perturbed location indicates better resolution. **d**  $V_C$  Hessian kernel map  
 290 indicating tradeoff between  $V_C$  and  $V_{SH}$ , where small kernel amplitudes indicate little or  
 291 no tradeoff.

292

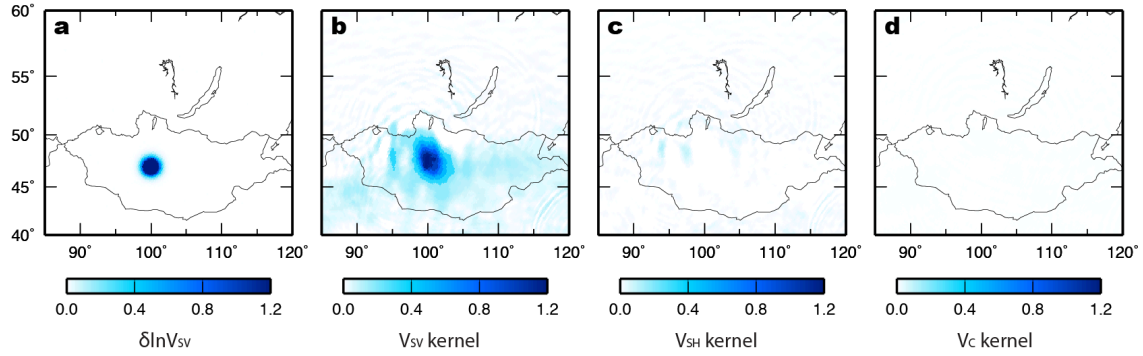
293

294

295

296

297



298

299 **Figure S2.** Resolution test of  $V_{SV}$  beneath Hangai Dome. **a** A 3D Gaussian spherical  
 300 perturbation in  $V_{SV}$  with a maximum strength of 4% at the center is placed at a depth of  
 301 300 km while  $V_{SH}$  and  $V_C$  remain unperturbed. **b**  $V_{SV}$  Hessian kernel map showing  
 302 imaging resolution of  $V_{SV}$ . **c**  $V_{SH}$  Hessian kernel map indicating tradeoff between  $V_{SH}$   
 303 and  $V_{SV}$ . **d**  $V_C$  Hessian kernel map indicating tradeoff between  $V_C$  and  $V_{SV}$ .

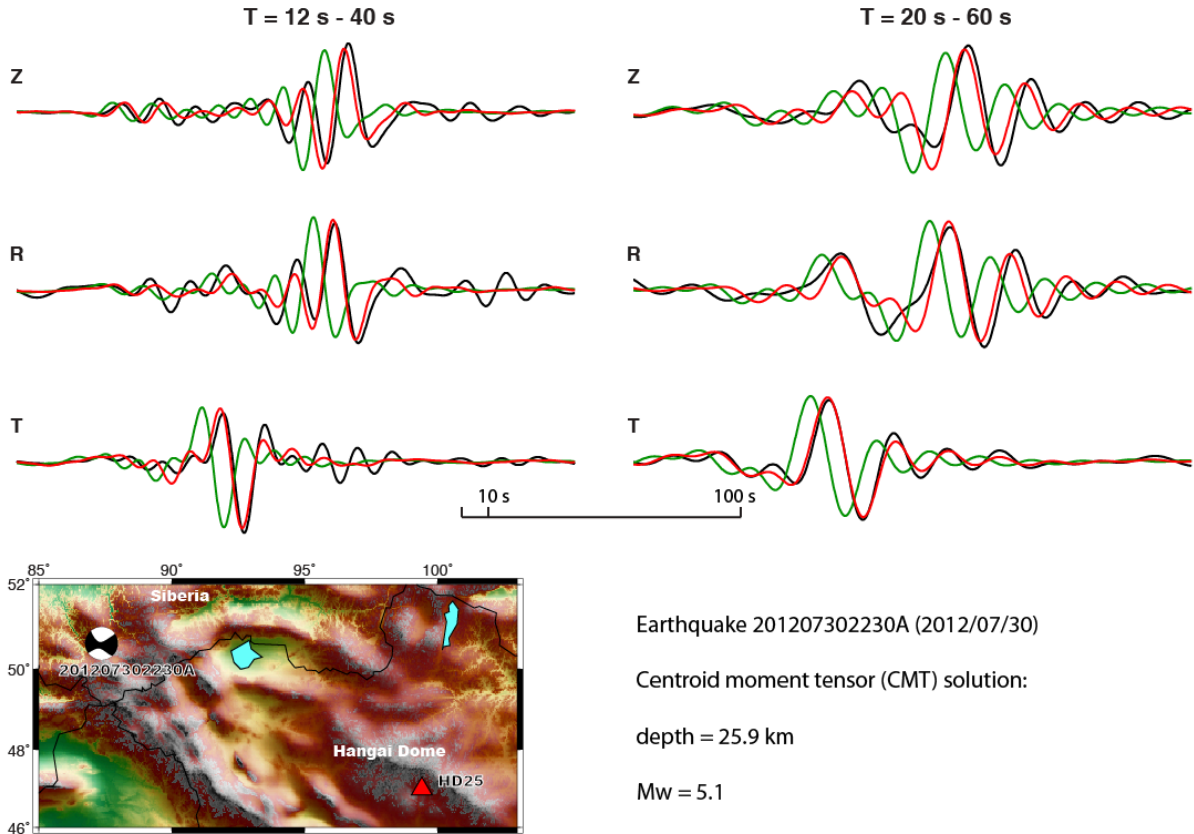
304

305

306

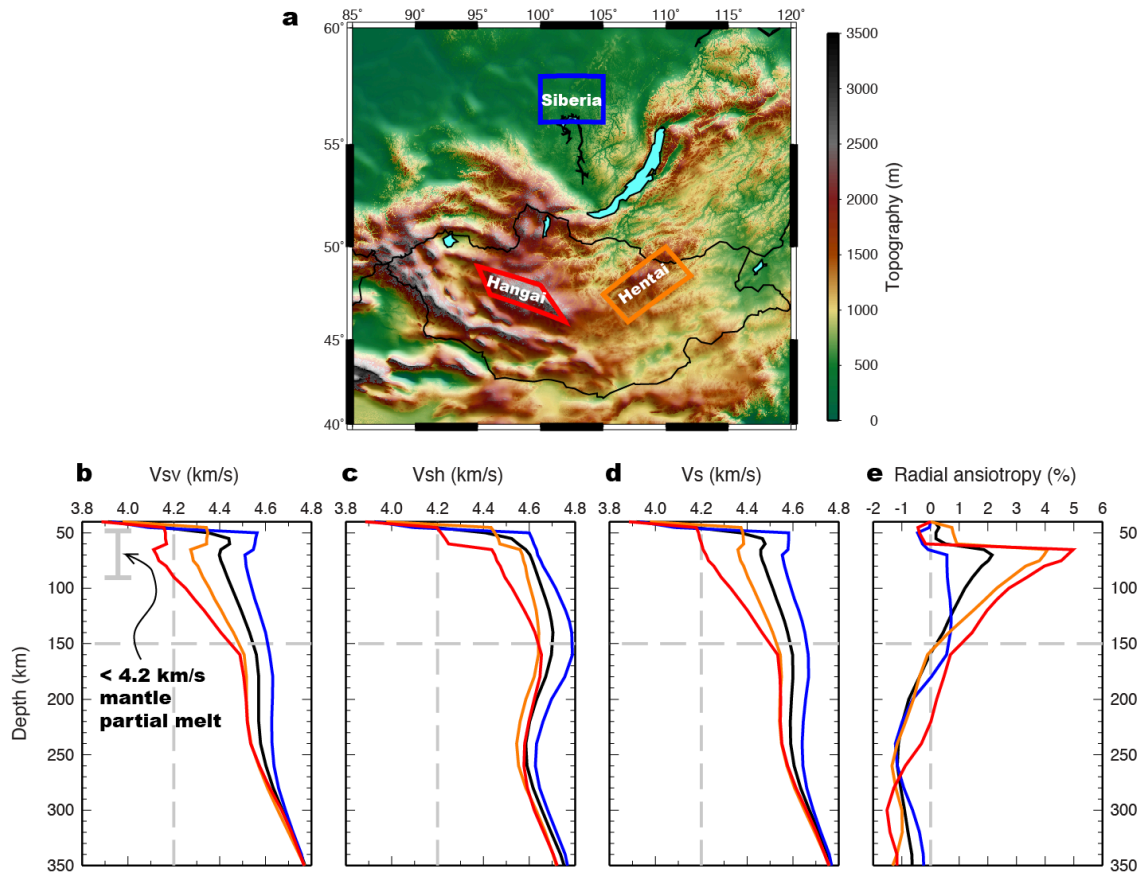
307

308



309

310 **Figure S3.** Examples of seismic waveform fitting. Map in the lower left shows the  
 311 selected earthquake (beach ball) and station (red triangle). Data (black lines), initial  
 312 model synthetics (green lines), and EARA2014 synthetics (red lines) are filtered in two  
 313 passbands with the period ranges of 12 s–40 s and 20 s–60s on all three components:  
 314 vertical (Z), radial (R), and tangential (T). Compared to the initial model synthetics,  
 315 EARA2014 synthetics have improved waveform fits in the Hangai Dome area. These  
 316 data were not used in the structural inversion.



317

318 **Figure S4.** Model analysis of EARA2014 under the Hangai-Hentai-Baikal area. a Map  
 319 region of the Hangai-Hentai-Baikal area in which the regional means of seismic  
 320 properties are calculated at each depth. The three polygons indicate the sampled area in  
 321 which the mean seismic properties of Hangai Dome (red polygon), Hentai Dome (orange  
 322 polygon), and Siberia (blue polygon), are calculated at each depth. Depth profiles for  
 323 Hangai Dome (red line), Hentai Dome (orange line), Siberia (blue line), and the entire  
 324 map region (black line) are shown for the mean  $V_{SV}$  in **b**, the mean  $V_{SH}$  in **c**, the mean  $V_S$  in  
 325 **d**, and the mean radial anisotropy in **e**. Horizontal gray dashed line at a depth of 150 km  
 326 is plotted as a reference to show the maximum depth extent of the low wavespeed (low-  
 327 V) region LV1 beneath Hangai Dome (with a seismic wavespeed reduction of  $-2\%$  or  
 328 more and positive radial anisotropy of  $1\%$  or more). Vertical gray dashed lines at a

329 seismic wavespeed of 4.2 km/s and a radial anisotropy of zero are also plotted as  
330 reference. Note that a low-V zone with wavespeeds less than 4.2 km/s (about a 7%  
331 reduction) exists on the mean  $V_{SV}$  depth profile of Hangai Dome over ~50 km–90 km  
332 depth range in **b**, indicating possible mantle partial melt due to decompression melting  
333 triggered magmatic underplating beneath the Moho. Also note that a zone of negative  
334 seismic wavespeed gradient indicative of the Lithosphere and Asthenosphere Boundary  
335 (LAB) only exists in  $V_{SH}$  profiles at depths around 200 km in **c** and is missing or not  
336 obvious in both  $V_{SV}$  (**b**) and  $V_S$  (**d**) profiles.

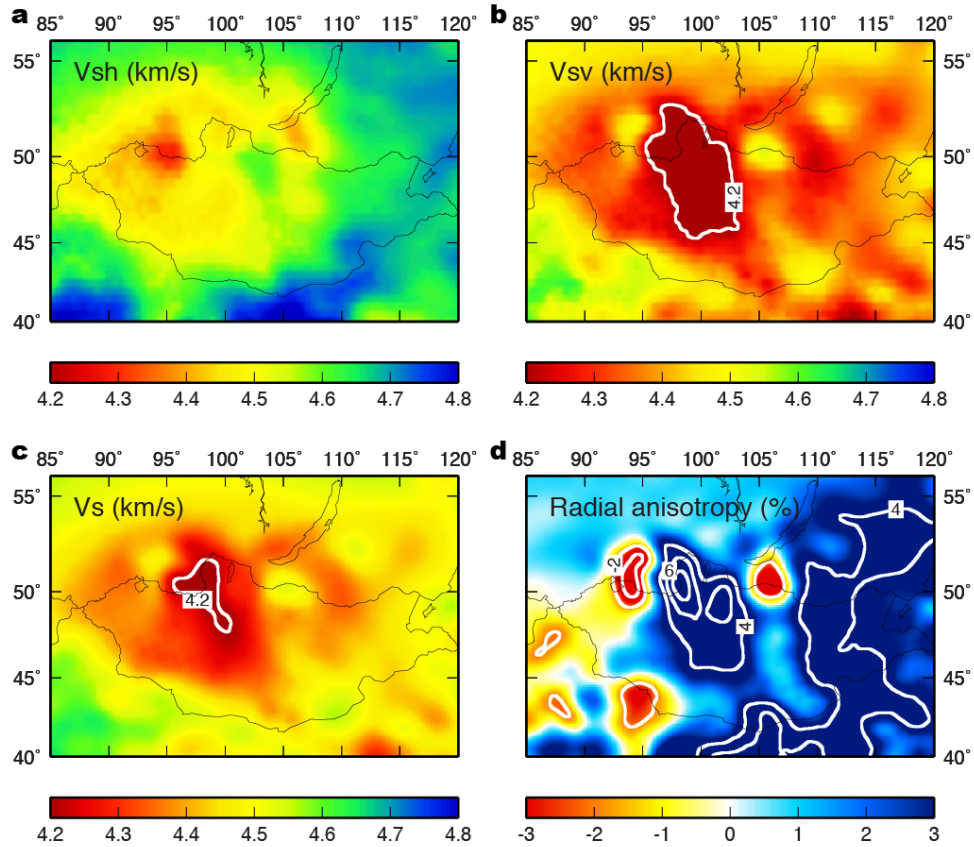
337

338

339

340

341



342

343 **Figure S5.** Map view of seismic structure at 80 km depth beneath the Hangai-Hentai-

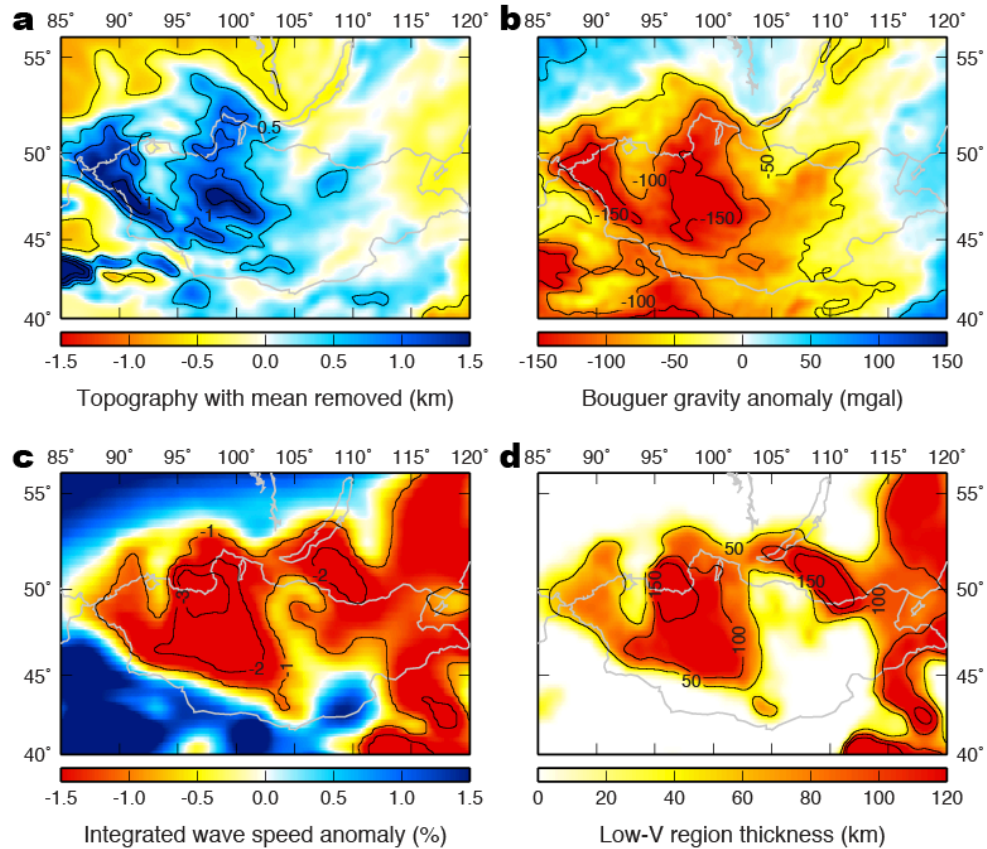
344 Baikal area. **a** Map of  $V_{SH}$ . **b** Map of  $V_{SV}$  with 4.2 km/s contour (white line). **c** Map of  $V_S$

345 with 4.2 km/s contour (white line). **d** Map of radial anisotropy with contours of -4%,

346 -2%, 4%, 6%, and 8% (white lines). Note that the contour of 4% radial anisotropy

347 correlates well with the contour of 4.2 km/s  $V_{SV}$  beneath Hangai Dome.

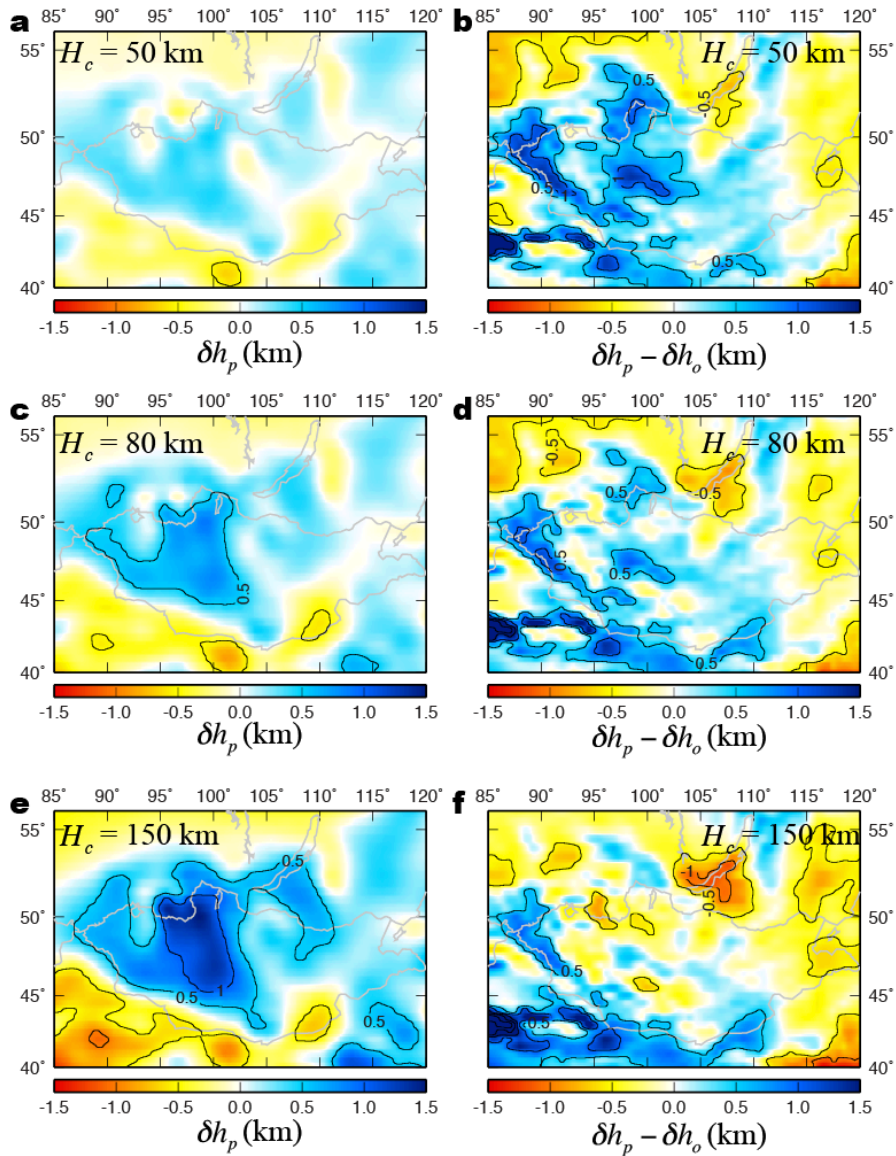
348



349

350 **Figure S6.** **a** Map view of topography. **b** Bouguer gravity anomalies. **c** Integrated  
 351 isotropic shear wavespeed anomalies from 0 km to 250 km depth normalized by  
 352 integrated depth. **d** column thickness of the low-V region in the upper 250 km with shear  
 353 wavespeed reduction larger than 2%. Black lines indicate contours in the maps. Note that  
 354 beneath Hangai Dome, the high topography, negative Bouguer gravity anomalies, low  
 355 integrated wavespeed anomaly, and thicker low-V columns are well correlated.

356



357

358 **Figure S7.** The predicted elevation variations ( $\delta h_p$ ) and the misfit ( $\delta h_p - \delta h_o$ ) between

359 the predicted  $\delta h_p$  and observed elevation variations  $\delta h_o$  using a scaling factor  $\zeta$  of 0.2 at

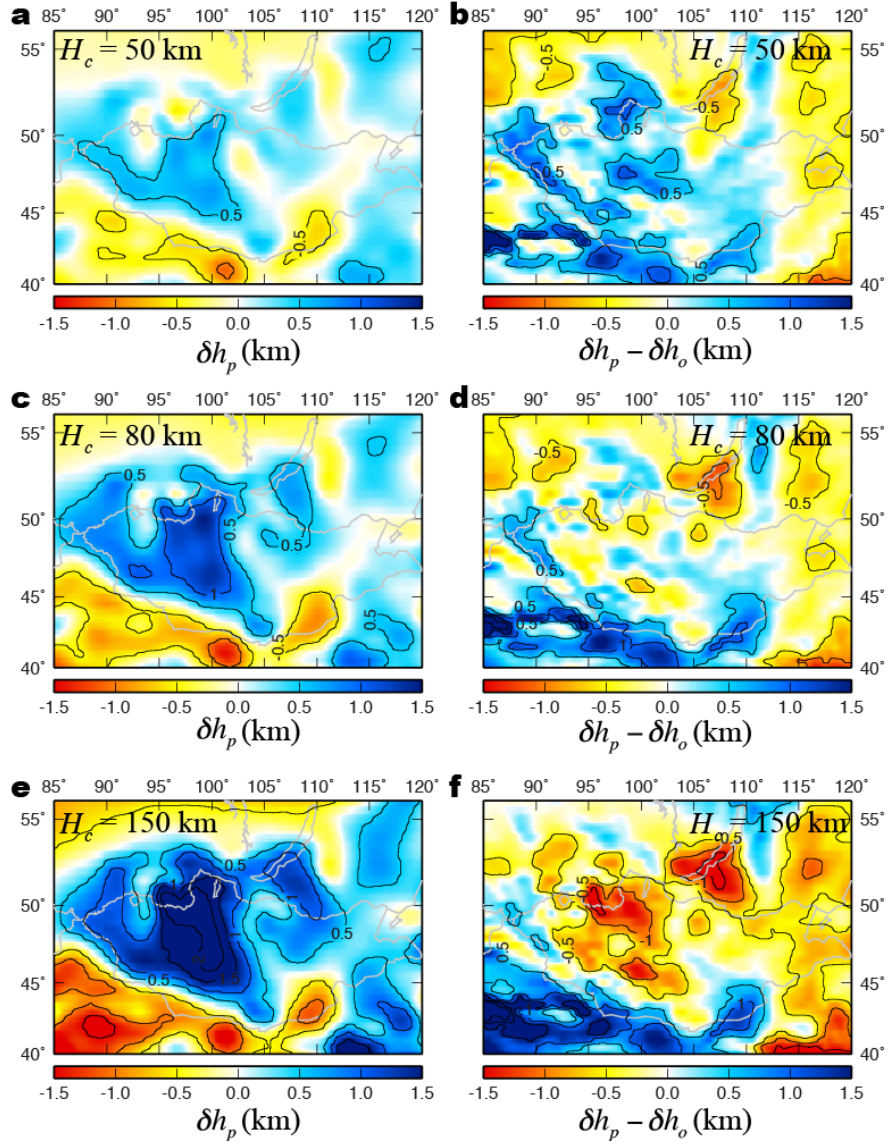
360 three different compensation depths:  $H_c$  of 50 km, 80 km, and 150 km.

361

362

363

364



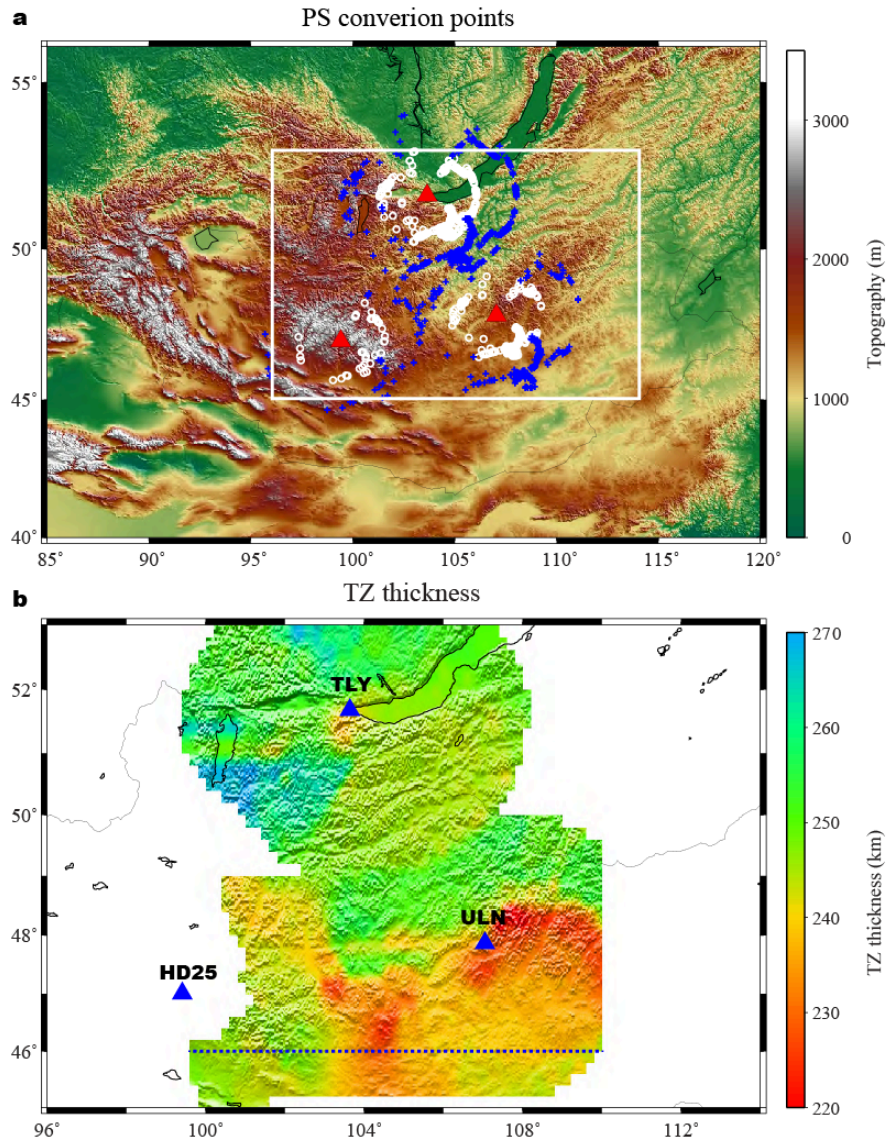
365

366 **Figure S8.** The predicted elevation variations ( $\delta h_p$ ) and the misfit ( $\delta h_p - \delta h_o$ ) between

367 the predicted  $\delta h_p$  and observed elevation variations  $\delta h_o$  using a scaling factor  $\zeta$  of 0.33

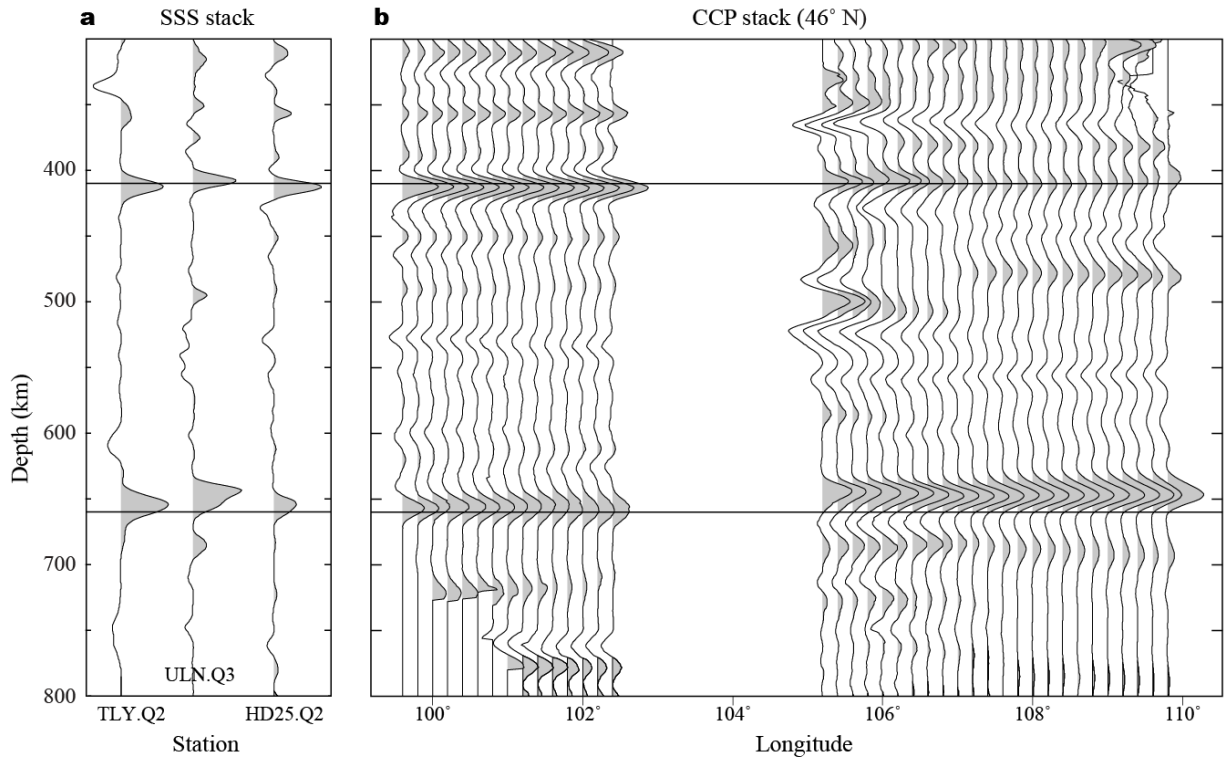
368 at three different compensation depths:  $H_c$  of 50 km, 80 km, and 150 km.

369



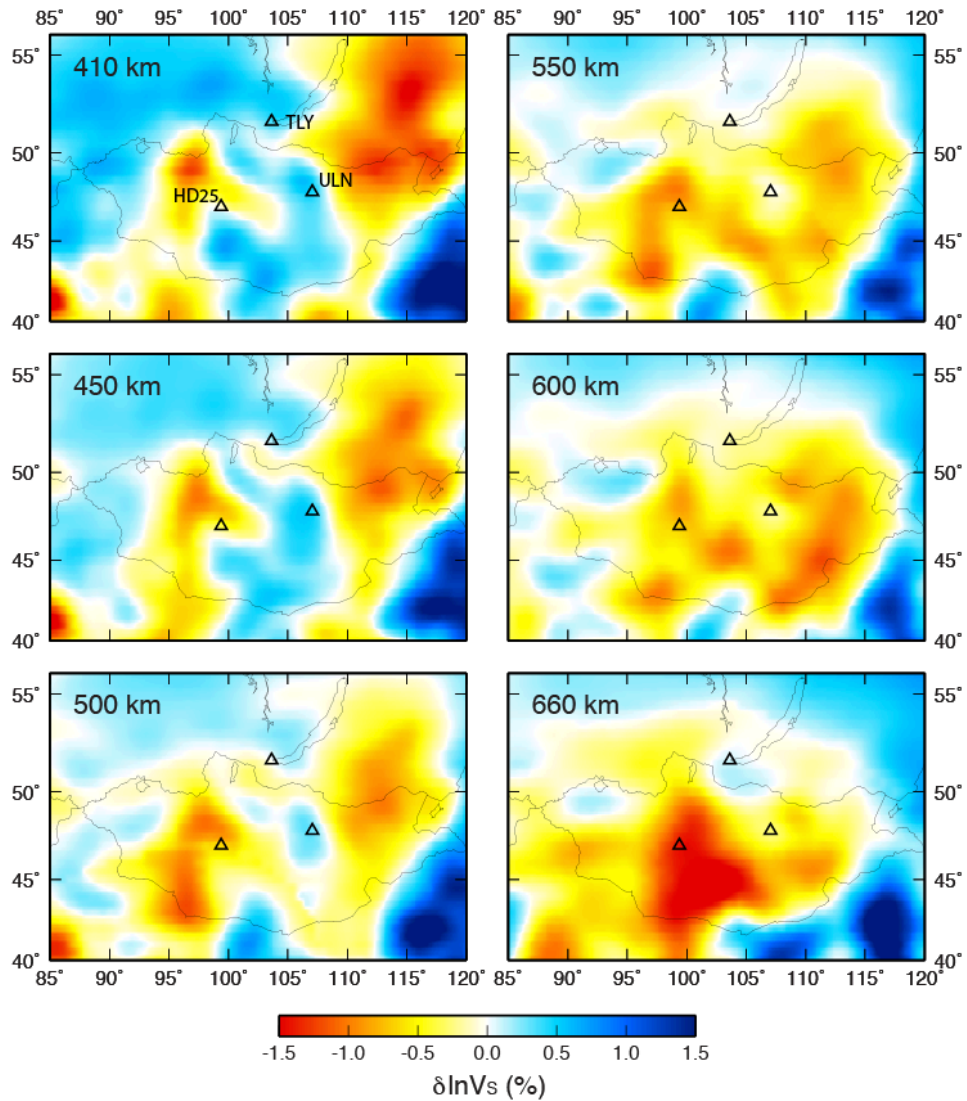
370

371 **Figure S9. a** Map showing two GSN stations (ULN and TLY) and one PASSCAL station  
 372 (HD25), together with the conversion points of the P410s (blue pluses) and P660s (white  
 373 circles). **b** Map of lateral variations of transition zone (TZ) thickness in an area  
 374 surrounding the 3 stations indicated by a white rectangle in **a** which are computed with  
 375 the 3-D EARA2014 model. The dashed line indicates the location of the CCP section  
 376 shown in Figure S10b.



377

378 **Figure S10. a** SSS stacks at the three stations. **b** CCP stacks along 46° N. The two  
 379 horizontal lines indicate the depths of the 410 and 660 discontinuities, respectively.



380

381 **Figure S11.** Maps of isotropic shear wavespeeds of EARA2014 at constant depths in the  
 382 mantle transition zone, in percent from the regional mean. The constant depth is shown in  
 383 the top left of each map. Three stations used in the receiver function analysis (HD25,  
 384 ULN, and TLY) (Figure S9b) are marked by triangles for reference. Note that the ~10  
 385 km–20 km thinner mantle transition zone (Figure S9b) area corresponds to the low  
 386 wavespeed anomalies in the vicinity of station HD25.

387

388 **Movie S1.** 360-degree rotating view of low wavespeed structures beneath the Hangai-  
389 Hentai-Baikal area.

390

391 **References**

392 Amante, C., and B. W. Eakins (2009), Etopo1 1 Arc-Minute Global Relief Model:  
393 Procedures, Data Sources and Analysis, *NOAA Tech. Memo. NESDIS NGDC-24*.  
394 *Natl. Geophys. Data Center, NOAA*, doi:10.7289/V5C8276M.

395 Anderson, D. L. (1987), A Seismic Equation of State II . Shear properties and  
396 thermodynamics of the lower mantle, *Phys. Earth Planet. Inter.*, *45*, 307–323.

397 Balmino, G., N. Vales, S. Bonvalot, and a. Briais (2012), Spherical harmonic modelling  
398 to ultra-high degree of Bouguer and isostatic anomalies, *J. Geod.*, *86*(7), 499–520,  
399 doi:10.1007/s00190-011-0533-4.

400 Bassin, C., G. Laske, and G. Masters (2000), The Current Limits of Resolution for  
401 Surface Wave Tomography in North America, *EOS Trans AGU*, *81*, F897.

402 Chen, M., F. Niu, Q. Liu, J. Tromp, and X. Zhen (2015), Multiparameter adjoint  
403 tomography of the crust and upper mantle beneath East Asia: 1. Model construction  
404 and comparisons, *J. Geophys. Res. Solid Earth*, *120*, doi:10.1002/2014JB011638.

405 Chen, Y., F. Niu, R. Liu, Z. Huang, H. Tkalčić, L. Sun, and W. Chan (2010), Crustal  
406 structure beneath China from receiver function analysis, *J. Geophys. Res.*,  
407 *115*(B03307), 1–22, doi:10.1029/2009JB006386.

408 Clayton, R. W., and R. A. Wiggins (1976), Source shape estimation and deconvolution of  
409 teleseismic bodywaves, *Geophys. J. R. Astron. Soc.*, *47*(1), 151–177,  
410 doi:10.1111/j.1365-246X.1976.tb01267.x.

411 Cox, K. G. (1993), Continental Magmatic Underplating, *Philos. Trans. R. Soc. A Math.*  
412 *Phys. Eng. Sci.*, *342*(1663), 155–166, doi:10.1098/rsta.1993.0011.

413 Dueker, K. G., and A. F. Sheehan (1997), Mantle discontinuity structure from midpoint  
414 stacks of converted P to S waves across the Yellowstone hotspot track, *J. Geophys.*  
415 *Res.*, *102*(B4), 8313–8327, doi:10.1029/96JB03857.

416 Ekström, G., A. M. Dziewoński, N. N. Maternovskaya, and M. Nettles (2005), Global  
417 seismicity of 2003: centroid–moment–tensor solutions for 1087 earthquakes, *Phys.*  
418 *Earth Planet. Inter.*, *148*(2-4), 327–351, doi:10.1016/j.pepi.2004.09.006.

- 419 Fichtner, A., and J. Trampert (2011), Hessian kernels of seismic data functionals based  
420 upon adjoint techniques, *Geophys. J. Int.*, *185*(2), 775–798, doi:10.1111/j.1365-  
421 246X.2011.04966.x.
- 422 Gilbert, H. J., A. F. Sheehan, K. G. Dueker, and P. Molnar (2003), Receiver functions in  
423 the western United States, with implications for upper mantle structure and  
424 dynamics, *J. Geophys. Res.*, *108*(B5), 2229, doi:10.1029/2001JB001194.
- 425 Karato, S. (1993), Importance of anelasticity in the interpretation of seismic tomography,  
426 *Geophys. Res. Lett.*, *20*(15), 1623–1626.
- 427 Kennett, B. L. N., and E. R. Engdahl (1991), Traveltimes for global earthquake location  
428 and phase identification, *Geophys. J. Int.*, *105*, 429–465, doi:10.1111/j.1365-  
429 246X.1991.tb06724.x.
- 430 Komatitsch, D., and J. Tromp (2002a), Spectral-element simulations of global seismic  
431 wave propagation — I . Validation, *Geophys. J. Int.*, *149*, 390–412,  
432 doi:10.1046/j.1365-246X.2002.01653.x.
- 433 Komatitsch, D., and J. Tromp (2002b), Spectral-element simulations of global seismic  
434 wave propagation — II . Three-dimensional models , oceans , rotation and self-  
435 gravitation, *Geophys. J. Int.*, *150*, 303–318, doi:10.1046/j.1365-246X.2002.01716.x.
- 436 Kustowski, B., G. Ekström, and a. M. Dziewoński (2008), Anisotropic shear-wave  
437 velocity structure of the Earth’s mantle: A global model, *J. Geophys. Res.*, *113*(B6),  
438 1–23, doi:10.1029/2007JB005169.
- 439 Liu, Q., and J. Tromp (2006), Finite-Frequency Kernels Based on Adjoint Methods, *Bull.*  
440 *Seismol. Soc. Am.*, *96*(6), 2383–2397, doi:10.1785/0120060041.
- 441 Liu, Q., and J. Tromp (2008), Finite-frequency sensitivity kernels for global seismic  
442 wave propagation based upon adjoint methods, *Geophys. J. Int.*, *174*(1), 265–286,  
443 doi:10.1111/j.1365-246X.2008.03798.x.
- 444 Liu, Q., J. Polet, D. Komatitsch, and J. Tromp (2004), Spectral-Element Moment Tensor  
445 Inversions for Earthquakes in Southern California, *Bull. Seismol. Soc. Am.*, *94*(5),  
446 1748–1761, doi:10.1785/012004038.
- 447 Liu, Z., and P. Bird (2008), Kinematic modelling of neotectonics in the Persia-Tibet-  
448 Burma orogen, *Geophys. J. Int.*, *172*(2), 779–797, doi:10.1111/j.1365-  
449 246X.2007.03640.x.
- 450 Liu, Z., F. Niu, Y. J. Chen, S. Grand, H. Kawakatsu, J. Ning, S. Tanaka, M. Obayashi,  
451 and J. Ni (2015), Receiver function images of the mantle transition zone beneath NE  
452 China: New constraints on intraplate volcanism, deep subduction and their potential  
453 link, *Earth Planet. Sci. Lett.*, *412*, 101–111, doi:10.1016/j.epsl.2014.12.019.

- 454 Maggi, A., C. Tape, M. Chen, D. Chao, and J. Tromp (2009), An automated time-  
455 window selection algorithm for seismic tomography, *Geophys. J. Int.*, 178(1), 257–  
456 281, doi:10.1111/j.1365-246X.2009.04099.x.
- 457 McKenzie, D. (1984), A possible mechanism for epeirogenic uplift, *Nature*, 307(5952),  
458 616–618, doi:10.1038/307616a0.
- 459 Muirhead, K. J. (1968), Eliminating False Alarms when detecting Seismic Events  
460 Automatically, *Nature*, 217, 533–534, doi:10.1038/217533a0.
- 461 National Geophysical Data Center (2006), 2-Minute Gridded Global Relief Data  
462 (ETOPO2v2), *World Data Serv. Geophys. U.S. Dep. Commer., NOAA, Boulder,*  
463 *Colo.* [Available <http://www.ngdc.noaa.gov/mgg/fliers/06mgg01.html>.].
- 464 Niu, F., and H. Kawakatsu (1998), Determination of the absolute depths of the mantle  
465 transition zone discontinuities beneath China: Effect of stagnant slabs on transition  
466 zone discontinuities, *Earth, Planets Sp.*, 50(11-12), 965–975,  
467 doi:10.1186/BF03352191.
- 468 Niu, F., A. Levander, S. Ham, and M. Obayashi (2005), Mapping the subducting Pacific  
469 slab beneath southwest Japan with Hi-net receiver functions, *Earth Planet. Sci. Lett.*,  
470 239, 9–17, doi:10.1016/j.epsl.2005.08.009.
- 471 Petit, C., J. De, and D. Fairhead (2002), Deep structure and mechanical behavior of the  
472 lithosphere in the Hangai-Hövsgöl region, Mongolia: new constraints from gravity  
473 modeling, , 197, 133–149.
- 474 Stachnik, J., A. Meltzer, S. Souza, and R. Russo (2014), Crustal and upper mantle  
475 structure of the Hangay Dome, central Mongolia, in *2014 IRIS Workshop Abstract*.
- 476 Tape, C., Q. Liu, A. Maggi, and J. Tromp (2009), Adjoint tomography of the southern  
477 California crust., *Science*, 325, 988–992, doi:10.1126/science.1175298.
- 478 Tromp, J., C. Tape, and Q. Liu (2005), Seismic tomography, adjoint methods, time  
479 reversal and banana-doughnut kernels, *Geophys. J. Int.*, 160(1), 195–216,  
480 doi:10.1111/j.1365-246X.2004.02453.x.
- 481 Vinnik, L. P. (1977), Detection of waves converted from P to SV in the mantle, *Phys.*  
482 *Earth Planet. Inter.*, 15(1), 39–45, doi:10.1016/0031-9201(77)90008-5.
- 483 Zheng, X., B. Ouyang, D. Zhang, Z. Yao, J. Liang, and J. Zheng (2009), Technical  
484 system construction of Data Backup Centre for China Seismograph Network and the  
485 data support to researches on the Wenchuan earthquake, *Chinese J. Geophys. (in*  
486 *Chinese)*, 52(5), 1412–1417, doi:10.3969/j.issn.0001-5733.2009.05.031.

487 Zhu, H., E. Bozdağ, D. Peter, and J. Tromp (2012), Structure of the European upper  
488 mantle revealed by adjoint tomography, *Nat. Geosci.*, 5(7), 493–498,  
489 doi:10.1038/ngeo1501.

490